Journal of Solid State Chemistry **145,** 541–548 (1999)
Article ID jssc.1999.8201, available online at http://www.idealibrary.com on IDEAL®

Structural Chemistry and Electronic Properties of Sr_2FeIrO_6

P. D. Battle,* G. R. Blake,* T. C. Gibb,† and J. F. Vente*

*Inorganic Chemistry Laboratory, Oxford University, South Parks Road, Oxford, OX1 3QR, United Kingdom; and
†School of Chemistry, Leeds University, Leeds, LS2 9JT, United Kingdom

Received October 5, 1998; accepted February 1, 1999

A polycrystalline sample of Sr_2FeIrO_6 has been synthesized and shown by a combination of X-ray diffraction, neutron diffraction, magnetometry, and Mössbauer spectroscopy to be a triclinic (space group $I\bar{1}$; $a = 5.54996(3)$ Å, $b = 5.57847(3)$ Å, $c = 7.84165(3)$ Å, $\alpha = 89.990(1)^\circ$, $\beta = 90.059(1)^\circ$, $\gamma = 90.079(1)^\circ$) perovskite, with a partially ordered (0.928 : 0.072(4)) distribution of transition metal cations over the six-coordinate sites. The predominant oxidation states are Fe^{3+} and Ir^{5+}, although the Mössbauer data suggest that $\sim 4\%$ Fe^{4+} is present. The compound is a Type II antiferromagnet below 120 K, with an ordered magnetic moment on the Fe-dominated sites of 3.67(3) μ_B per Fe^{3+} cation. The spins associated with the antisite defects are frustrated and do not take part in the long-range magnetic ordering, consequently giving rise to hysteresis in the magnetic susceptibility below 40 K. The possible location of the Fe^{4+} cations is discussed briefly.

INTRODUCTION

In recent years, the solid-state chemistry of mixed-metal oxides containing platinum group metals has attracted a great deal of interest. These materials adopt a diverse range of structures, with a correspondingly wide range of electronic properties being displayed. Of late, we have focused our attention on the structural chemistry and magnetic properties of iridium oxides, as have a number of other research groups. Various mixed-metal iridates with the perovskite structure or a slight distortion thereof have been reported, with iridium taking the oxidation states Ir(IV), Ir(V), or Ir(VI). Examples include the Ir(IV) compound $La_2Zn_xMg_{1-x}IrO_6$ (1), which exhibits ferromagnetism for $x = 1$ and antiferromagnetism for $x = 0$, and the Ir(VI) phases Ba_2CaIrO_6 (2) and Sr_2CaIrO_6 (3), which are both antiferromagnetic at low temperatures. Ir(V) is nonmagnetic with a $j = 0$ ground state, and perovskites, for example (4) $BaLaMgIrO_6$, in which Ir(V) is the only transition-metal cation, do not show long-range magnetic order. The 6-coordinate sites in all of these compounds are occupied by an ordered 1 : 1 distribution of Ir and a diamagnetic, divalent cation. When the latter is replaced by a transition metal cation the interpretation of magnetic data can become more complex. Sometimes the additional complexity simply stems from the presence of two magnetic cations, but there can also be an ambiguity in the cation oxidation states present; a combination of X-ray diffraction, neutron diffraction, and magnetometry was necessary to show that $BaLaCoIrO_6$ (5, 6) contains a 1 : 1 ordered arrangement of Co^{2+}/Ir^{5+} rather than Co^{3+}/Ir^{4+}. The additional complications introduced by the possibility of either a high-spin (paramagnetic) or a low-spin (diamagnetic) configuration for Co^{3+} also had to be taken into account in this case. The nature of the magnetic interaction between Ir and the second transition metal will depend on the occupancy of the two sets of *d* orbitals and the degree of order in the distribution of the cations over the 6-coordinate sites. The observation of a spontaneous magnetization in La_2CoIrO_6 (7) suggests that it may be possible to prepare new ferromagnetic oxides by controlling the structural ordering of different cations with the appropriate *d*-electron configurations. The importance of structural ordering is emphasized by X-ray diffraction and susceptibility data which suggest (6, 7) that whereas long-range magnetic order is found at low temperatures in compounds, for example La_2CoIrO_6 and La_2NiIrO_6, in which Ir(IV) and M^{2+} maintain a 1 : 1 ordered array, spin-glass behavior is observed in compounds, for example $BaLaFeIrO_6$, which contain a random distribution of transition metal cations. In general, long-range magnetic order is most likely to occur in a compound of the general formula $AA'BB'O_6$ when the 6-coordinate cations *B* and *B'* are structurally ordered. In turn, this is most likely when the differences in charge and size between the cations is large.

The varied behavior described above is not found only in compounds of Ir. A variation in the degree of $Fe^{3+} : M^{5+}$ ordering causes Sr_2FeMO_6 to be a spin glass ($T_g = 23$ K) for $M = Ta$ (8, 9), an antiferromagnet with incomplete spin ordering ($T_N = 36$ K) for $M = Sb$ (8–10), and a fully ordered antiferromagnet ($T_N = 91$ K) for $M = Bi$ (11). When diamagnetic Ta^{5+}, Sb^{5+}, or Bi^{5+} is replaced by paramagnetic Ru^{5+}, disorder in the cation distribution again (12) frustrates the formation of an antiferromagnetic

0022-4596/99 $30.00

low-temperature state, despite the high concentration of magnetic cations. The complex electronic properties of both Fe and Ir perovskites motivated us to prepare and characterize the new material Sr_2FeIrO_6, which contains the pair of elements at the center of the above discussion. The cation oxidation states, the extent of structural cation ordering, and the magnetic properties of this compound have been determined by a combination of Mössbauer spectroscopy, X-ray diffraction, neutron diffraction, and magnetometry. Our results are discussed in the light of the previous work.

EXPERIMENTAL

A polycrystalline ($\sim$10 g) sample of nominal metal content 2Sr : Fe : Ir was prepared by heating stoichiometric quantities of $SrCO_3$, Fe_2O_3, and Ir metal in an alumina crucible. The reaction mixture was initially heated overnight at 800°C, then reground, pelletized, and heated in air at 975°C (5 days), 1050°C (5 days), 1100°C (8 days), and 1150°C (6 days). The reaction mixture was reground frequently, and progress was followed by powder X-ray diffraction (XRD). The reaction was deemed to be complete when a monophasic product of good crystallinity was obtained. XRD data were collected at room temperature using a Siemens D5000 diffractometer, operating with Cu$K\alpha_1$ radiation in Bragg–Brentano geometry over the angular range $5 \leq 2\theta/^\circ \leq 120$, with a 2θ step size of 0.02°. The metal content of the product was analyzed using an Atomscan 25 ICP emission spectrometer. The oxygen content was determined by thermogravimetric analysis using 10%H_2/N_2 as the reducing agent in a Rheometric Scientific STA 1500, the sample being heated to 900°C. The reaction product was also characterized by time-of-flight neutron diffraction. Data were collected on the HRPD and IRIS instruments at the ISIS facility, Rutherford–Appleton Laboratory. The HRPD data were collected in the d-spacing range $0.68 \leq d/\text{Å} \leq 2.5$ on a sample of mass $\sim$4 g contained in a cylindrical vanadium can at room temperature and were used for a detailed investigation of the crystal structure. The IRIS data were collected on a sample of mass $\sim$3 g over a d-spacing range of $1.5 \leq d/\text{Å} \leq 9.4$ in a vanadium can at 5 K, and were used to investigate the magnetic structure. All the X-ray and neutron diffraction data were analyzed using the GSAS program package (13). The neutron diffraction data were corrected for absorption effects, as the absorption cross section for iridium compounds is large. The background levels of the XRD, HRPD, and IRIS diffraction profiles were modeled by Chebyschev polynomials of the first kind (12, 7, and 10 parameters respectively). In the case of HRPD and IRIS, the peak shape was described by a convolution of back-to-back exponentials and a pseudo-Voigt function (three parameters); the shape of the X-ray diffraction peaks was described by a five-parameter pseudo-Voigt function. Magnetic susceptibility measurements were made using a Quantum Design MPMS-5 SQUID magnetometer. Zero-field-cooled (ZFC) and field-cooled (FC) data were collected after cooling the sample, mounted in a gelatin capsule, to 5 K in zero field and in the measuring fields of 100 and 1000 G. Measurements of magnetization versus field were also carried out, the field being cycled between 5000 and $-$5000 G at temperatures of 300, 40, 20, 10, and 5 K after cooling in a field of 5000 G. Electrical conductivity measurements were made using the standard four-probe dc technique, conducting silver paint being used to attach copper wires to a sintered bar of the sample.

Mössbauer spectra were collected at room temperature using a ^{57}Co/Rh source matrix, also held at room temperature. Isomer shifts were calibrated relative to metallic iron.

RESULTS

ICP analysis for the metal content of our reaction product gave the following weight percentages of each element; the values expected for the ideal composition of Sr_2FeIrO_6 are given in brackets: Sr, 34.89% (33.74%); Fe, 11.19% (10.75%); Ir, 38.58% (37.01%). The experimental values lead to compositions close to those expected, confirming that no significant metal loss has occurred during the preparations. TGA analysis for oxygen content showed that the weight loss on heating to 900°C in 10% H_2/N_2 was 12.34%, corresponding to a composition of $Sr_2FeIrO_{6.004}$ if ideal metal contents are assumed. Therefore, the composition of our reaction product is Sr_2FeIrO_6, within the bounds of experimental error.

The powder XRD pattern of Sr_2FeIrO_6 could be indexed in a monoclinic unit cell, of dimensions similar to those of the high-pressure form of Sr_2CaIrO_6 (5). A Rietveld refinement of the crystal structure proceeded smoothly in space group $P2_1/n$. The agreement between the observed and calculated diffraction profiles was improved substantially by allowing a small degree of disorder in the iridium/iron distribution. Refinement of the HRPD neutron diffraction data using this model resulted in unsatisfactory agreement between the observed and calculated profiles. Furthermore, one of the iridium–oxygen bond distances was unreasonably short at 1.85 Å. A reduction of the symmetry, using the nonstandard triclinic space group $I\bar{1}$, yielded more satisfactory bond distances and a better agreement between the observed and calculated profiles. However, as the neutron scattering lengths of iridium and iron are similar, the refinement was very insensitive to the degree of iridium/iron disorder. A refinement was therefore carried out using both the X-ray and neutron diffraction data simultaneously. Due to an imperfect correction for absorption in the neutron diffraction data, isotropic temperature factors consistent with both data sets could not be refined. This problem was overcome by including two phases, one assigned to the XRD data and the other to the neutron diffraction data.

The two phases were allowed different temperature factors but were constrained to be identical in all other respects as their structure was refined. In the space group $I\bar{1}$ there are two crystallographically distinct six-coordinate sites, one mainly occupied by iron and one by iridium. These will be referred to subsequently as the 2*b* and 2*c* sites, located at (0, 0.5, 0) and (0.5, 0, 0), respectively. The proportion of iron on the 2*b* site refined to 92.8(4)%, with 7.2(4)% iridium, and the 2*c* site had the complementary distribution. The refinement converged smoothly with one set of lattice parameters and atomic coordinates and two distinct sets of isotropic temperature factors. The agreement between the observed and calculated diffraction profiles is good ($R_{wpr} = 7.11\%$ for the combined data sets); the X-ray and neutron diffraction profiles are shown in Fig. 1, the refined atomic coordinates are presented in Table 1, and the bond distances and angles are summarized in Tables 2 and 3, respectively. A representation of the refined crystal structure is given in Fig. 2.

The observed and fitted ^{57}Fe Mössbauer spectra at 290 K are shown in Fig. 3. The observed spectrum consists of a broad single line with no resolved quadrupole splitting. The isomer shift is $\delta = 0.4535(7)\ \text{mm s}^{-1}$ and the linewidth is $\Gamma = 0.416(2)\ \text{mm s}^{-1}$. The isomer shift indicates that iron is present as Fe^{3+}, the value of δ being only slightly higher than that ($0.423\ \text{mm s}^{-1}$) reported for Fe^{3+} in Sr_2FeSbO_6 (10), a monoclinic perovskite in which Fe^{3+} and Sb^{5+} are partially ordered, and that ($0.389\ \text{mm s}^{-1}$) of Sr_2FeBiO_6 (11), described on the basis of X-ray diffraction data as a cubic perovskite with full cation ordering. There is a slight misfit on the low-velocity edge of the main line, at $\delta = 0.017(11)\ \text{mm s}^{-1}$, which may be accounted for by the presence of around 4% Fe^{4+}.

The molar magnetic susceptibility and the inverse molar magnetic susceptibility of Sr_2FeIrO_6 are plotted against temperature in Figs. 4a and 4b. A transition to antiferromagnetic ordering is seen with a Néel temperature of 120 K. At temperatures above 230 K the data could be fitted to the Curie–Weiss law, with $C = 4.68(5)\ \text{emu K mol}^{-1}$ and $\theta = -190(5)$ K in a measuring field of 1000 G. The value of the magnetic moment calculated from the Curie constant ($6.12\ \mu_B$) is consistent with the presence of Fe^{3+}/Ir^{5+}. Only Fe^{3+} would contribute to the magnetic moment because,

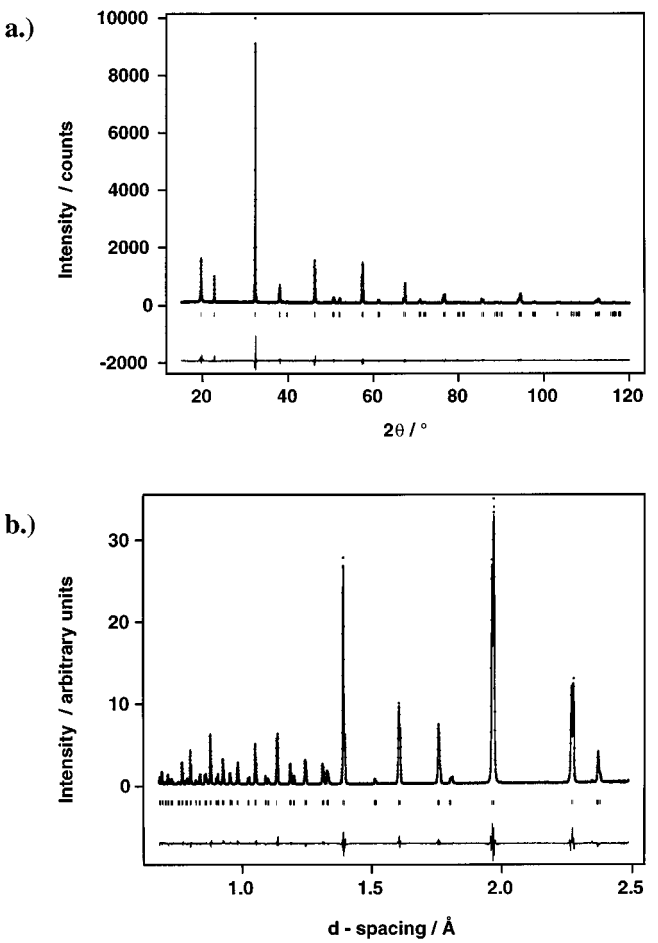

FIG. 1. Observed, calculated, and difference room temperature diffraction profiles for Sr_2FeIrO_6: (a) X-ray data; (b) HRPD neutron data. Reflection positions are marked.

TABLE 1
Atomic Parameters for Sr_2FeIrO_6 at Room Temperature

Atom	Site	Occupancy[a]	*x*	*y*	*z*	U_{iso}[b] (Å^2)	U_{iso}[c] (Å^2)
Sr			0.4998(9)	0.4993(4)	0.2501(6)	0.0067(2)	0.025(1)
Fe	2*b*	0.928(4)	0	0.5	0	−0.0001(9)	0.015(2)
Ir	2*c*	0.928(4)	0.5	0	0	0.005(1)	0.0184(9)
O1			0.2596(9)	0.260(1)	0.9848(6)	0.0088(7)	0.040(9)
O2			0.2475(10)	0.756(2)	0.0242(5)	0.0102(8)	0.040(9)
O3			0.5012(9)	0.0386(3)	0.250(1)	0.0092(4)	0.040(9)

Note. Space group $I\bar{1}$: $a = 5.54996(3)$ Å, $b = 5.57847(3)$ Å, $c = 7.84165(3)$ Å, $\alpha = 89.990(1)^\circ$, $\beta = 90.059(1)^\circ$, $\gamma = 90.079(1)^\circ$, $V = 242.779(1)$ Å^3. HRPD data: $R_{wpr} = 6.78\%$, $R_{pr} = 5.66\%$. XRD data: $R_{wpr} = 8.85\%$, $R_{pr} = 6.85\%$. Combined refinement: $R_{wpr} = 7.11\%$, $R_{pr} = 6.71\%$, $\chi^2 = 5.224$.

[a] Fe fraction + Ir fraction = 1.

[b] From neutron diffraction.

[c] From X-ray diffraction.

TABLE 2
Bond Lengths for Sr_2FeIrO_6 at Room Temperature

Fe–O1	1.971(7) × 2	Sr–O1	2.807(7)	Sr–O1	2.641(6)
Fe–O2	1.991(8) × 2	Sr–O1	2.752(6)	Sr–O1	2.914(6)
Fe–O3	1.973(9) × 2	Sr–O2	2.675(6)	Sr–O2	2.940(7)
Ir–O1	1.977(7) × 2	Sr–O2	2.888(6)	Sr–O2	2.624(7)
Ir–O2	1.960(8) × 2	Sr–O3	2.570(2)	Sr–O3	3.009(2)
Ir–O3	1.972(9) × 2	Sr–O3	2.778(7)	Sr–O3	2.788(7)

as stated above, Ir^{5+} is expected to have a nonmagnetic ($j = 0$) ground state when in a crystal field with cubic symmetry. As the temperature falls to ca. 50 K, well below T_N, both the FC and ZFC susceptibilities begin to rise again, and at around 40 K the FC and ZFC susceptibilities begin to diverge slightly. The ZFC data show a maximum at 7 K, close to the limit of the measured temperature range. The susceptibility showed no significant dependence on the measuring field. The field dependence of the isothermal magnetisation was measured at temperatures between 5 and 40 K. No strong hysteresis was apparent but a positive remnant magnetisation was observed at zero applied field (Fig. 5). This effect was very slight at 40 K but became more significant at lower temperatures.

A Rietveld refinement of the magnetic structure of Sr_2FeIrO_6 at 5 K was carried out using the crystallographic model obtained from the combined refinement of X-ray and HRPD data collected at room temperature. The free-ion magnetic form factor of Fe^{3+} (14) was used to describe the angular dependence of the magnetic scattering amplitude. The magnetic Bragg peaks observed in the low-temperature IRIS data could be accounted for only by a Type II (15) spin structure involving a single six-coordinate site. The magnetic scattering was assumed to come wholly from Fe^{3+}, and consequently no ordered moment was assigned to the Ir-rich 2*c* site. The Type II cell is derived from the crystallographic cell by doubling the lattice parameters along each axis. Magnetic moments align ferromagnetically in sheets parallel to the (011) plane of the doubled unit cell, adjacent sheets coupling antiferromagnetically. The lattice parameters were refined, but since data were collected at *d* spacings above 1.5 Å there were too few nuclear Bragg peaks to refine the atomic coordinates, which were consequently held at their room temperature values. An overall isotropic temperature factor was refined. The ordered components of the magnetic moment of Fe^{3+} were allowed to vary; the components along the crystallographic axes refined to be $m_x = 0.44(12)\,\mu_B$, $m_y = 1.48(28)\,\mu_B$, and $m_z = -3.33(11)\,\mu_B$, with the net moment having a magnitude of $3.67(3)\,\mu_B$. The standard deviations of these parameters show that the magnitude of the moment is well defined, although the direction is not. The final observed, calculated, and difference diffraction profiles are shown in Fig. 6. The principal features in the difference profile occur at the positions of structural Bragg peaks and reflect the small changes in the atomic positions which occur between room temperature and 5 K. Figure 7 is a schematic illustration of the ordered moments in the Type II magnetic unit cell. Electrical conductivity measurements on a polycrystalline sintered bar showed that Sr_2FeIrO_6 is a semiconductor with a room temperature conductivity of $26\,\Omega^{-1}\,cm^{-1}$. A plot of electrical conductivity versus temperature is shown in Fig. 8a.

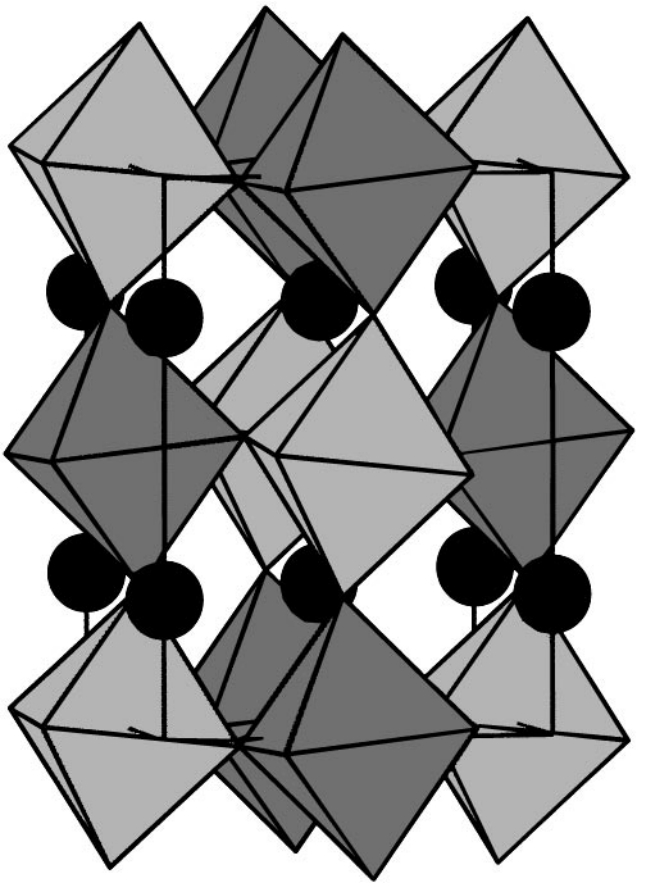

FIG. 2. Crystal structure of Sr_2FeIrO_6. Lightly shaded octahedra are occupied by 93% Fe^{3+}; darkly shaded octahedra are occupied by 93% Ir^{5+}. Black circles represent Sr^{2+}.

TABLE 3
Bond Angles for Sr_2FeIrO_6 at Room Temperature

O1–Fe–O2	89.4(3)
O1–Fe–O3	89.4(2)
O2–Fe–O3	89.2(2)
O1–Ir–O2	88.2(3)
O1–Ir–O3	88.9(2)
O2–Ir–O3	88.9(2)
Fe–O1–Ir	171.7(3)
Fe–O2–Ir	168.8(2)
Fe–O3–Ir	167.5(1)

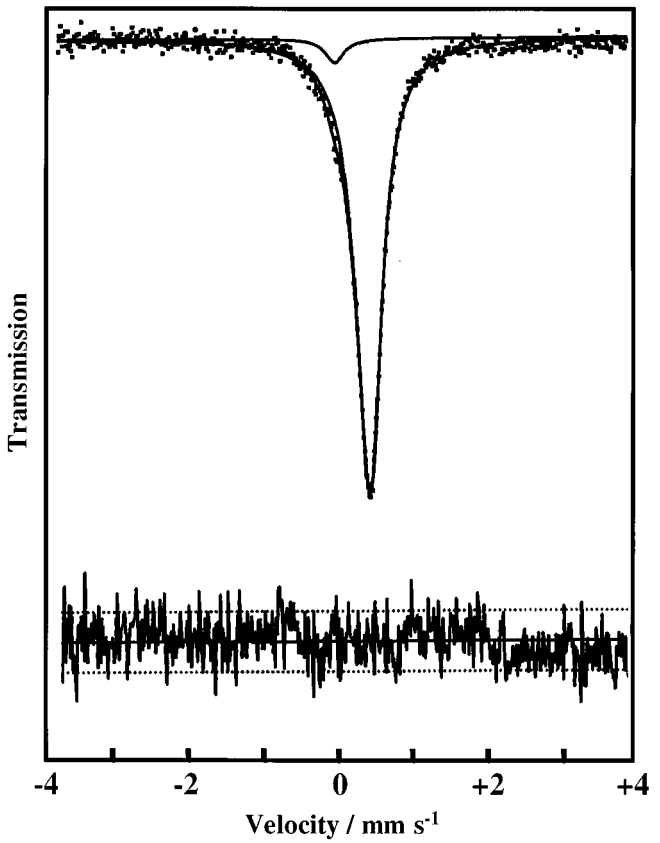

FIG. 3. Observed and fitted ^{57}Fe Mössbauer spectra of Sr_2FeIrO_6 at 290 K.

The relationship between $\ln \sigma$ and $1/T$ (Fig. 8b) is not linear, the activation energy decreasing from 58(1) meV at 290 K to 16.4(3) meV at 90 K.

DISCUSSION

The Mössbauer spectrum and the magnetic susceptibility data described above are both consistent with the assignment of the cation oxidation states in Sr_2FeIrO_6 as Fe^{3+} and Ir^{5+}. Our new phase is thus an example of a quarternary perovskite containing Fe^{3+} as the sole cation with a magnetic ground state. The octahedral coordination around both six-coordinate sites is distorted from the ideal, as is shown by the tabulated bond lengths and bond angles. Neutron diffraction proved to be crucial in the structural characterization of this compound because it was able to detect the small displacements of the oxide ions from their ideal positions. These displacements decrease the overall symmetry below that apparent from the X-ray diffraction data. Judged on the basis of the sensitivity of the Mössbauer quadrupole splitting to the degree of B/B' cation order, established previously (8) by comparison of the markedly different spectra of Sr_2FeTaO_6 (disordered Fe/Ta) and Sr_2FeSbO_6 (partially ordered Fe/Sb), the unsplit Mössbauer spectrum of Sr_2FeIrO_6 suggests a high degree of Fe/Ir ordering. However, after consideration of our XRD and magnetic data we conclude that there is some disorder present, with the 2*b* sites of $Sr_2BB'O_6$ occupied by 93% iron and 7% iridium, and vice versa on the 2*c* sites. The agreement between the observed and calculated XRD profiles showed a clear improvement on the introduction of disorder. At room temperature, the average Fe/Ir–O bond length at the Ir-dominated site is 1.969 Å, similar to that reported for the ordered Ir(V) perovskite $BaLaCoIrO_6$ (5), and the mean distance (1.978 Å) at the other six-coordinate site is reasonable for Fe(III). Further evidence of cation disorder is found in the rise in magnetic susceptibility below 50 K, which can be taken to indicate that a small proportion of Fe moments are not antiferromagnetically coupled below T_N, but remain disordered. The divergence of the FC and

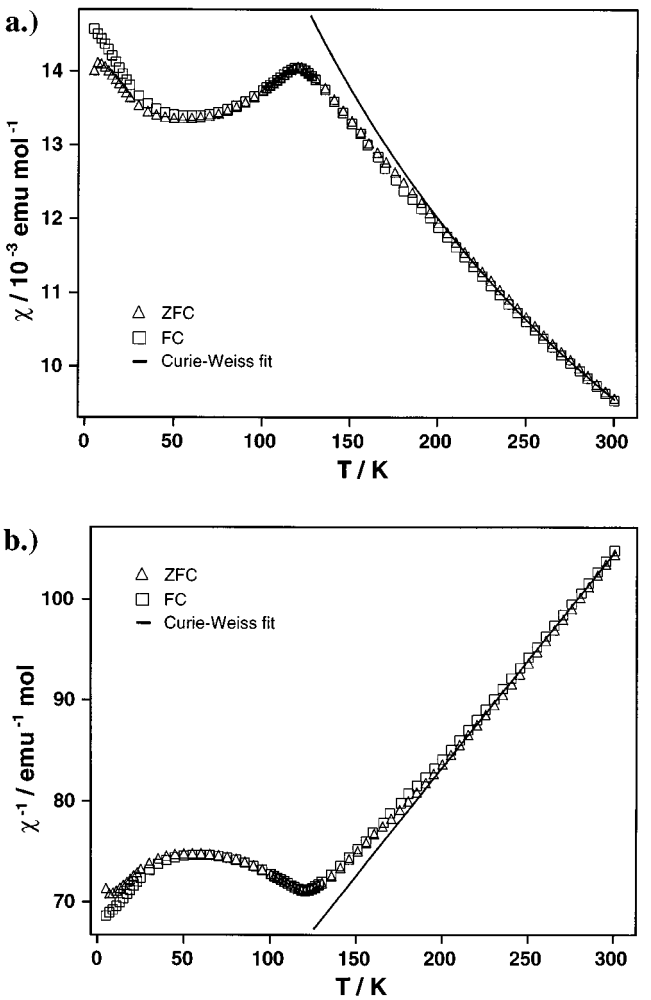

FIG. 4. (a) Molar magnetic susceptibility and (b) inverse magnetic susceptibility of Sr_2FeIrO_6 measured in 1000 G as a function of temperature. A fit to the Curie–Weiss law is shown above 230 K.

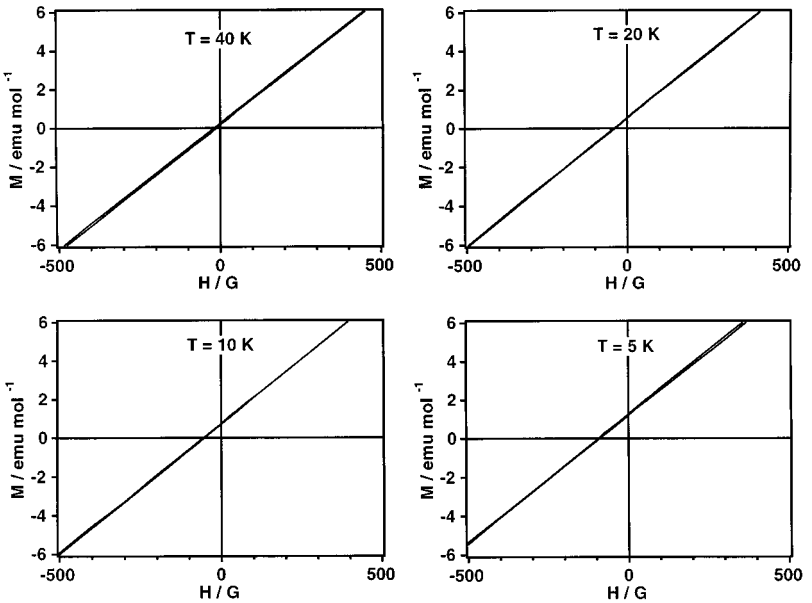

FIG. 5. Magnetization of Sr_2FeIrO_6 as a function of field and temperature.

ZFC susceptibilities below 40 K is likely to be due to short-range order among these disordered spins, as is the displacement of the $M(H)$ curve away from the origin. The low value of the average ordered magnetic moment of Fe^{3+} in Sr_2FeIrO_6 is also consistent with the disordered model. The expected value of the ordered magnetic moment, observed in an ideal antiferromagnetic oxide of Fe^{3+} after taking a degree of covalency into account, is $\sim 4.4\ \mu_B$ (16), significantly larger than our refined value of $3.67(3)\ \mu_B$. The reduced magnetic moment suggests that a proportion of the sites on the sublattice nominally occupied by Fe do not contain ordered moments. This is consistent with their occupation by nonmagnetic Ir^{5+}. However, the extent of the moment reduction is surprisingly large for the amount

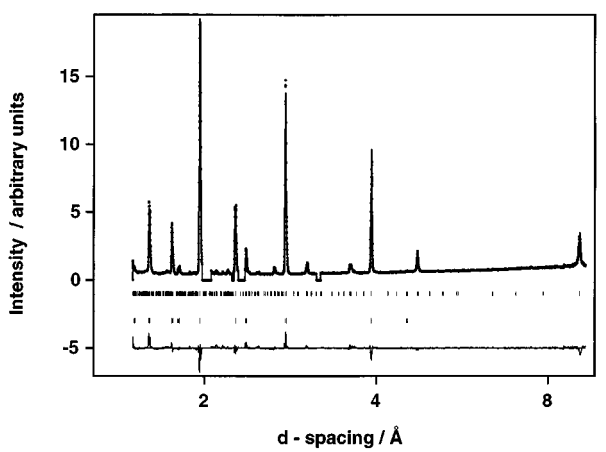

FIG. 6. Observed, calculated, and difference diffraction profiles for Sr_2FeIrO_6 (IRIS data). Data were collected at 5 K. Reflection positions for the magnetic (upper tick marks) and crystallographic (lower tick marks) structures are indicated. Profile regions contaminated by cryostat peaks were excluded from the refinement.

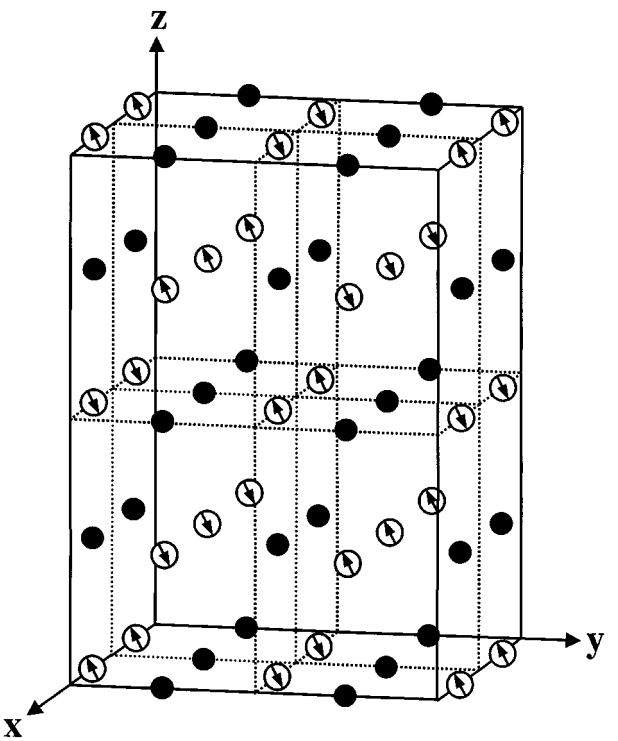

FIG. 7. Schematic representation of the Type II magnetic unit cell. Open circles with arrows indicate the position and direction of the Fe^{3+} moments. Black circles indicate the positions of nonmagnetic Ir^{5+}.

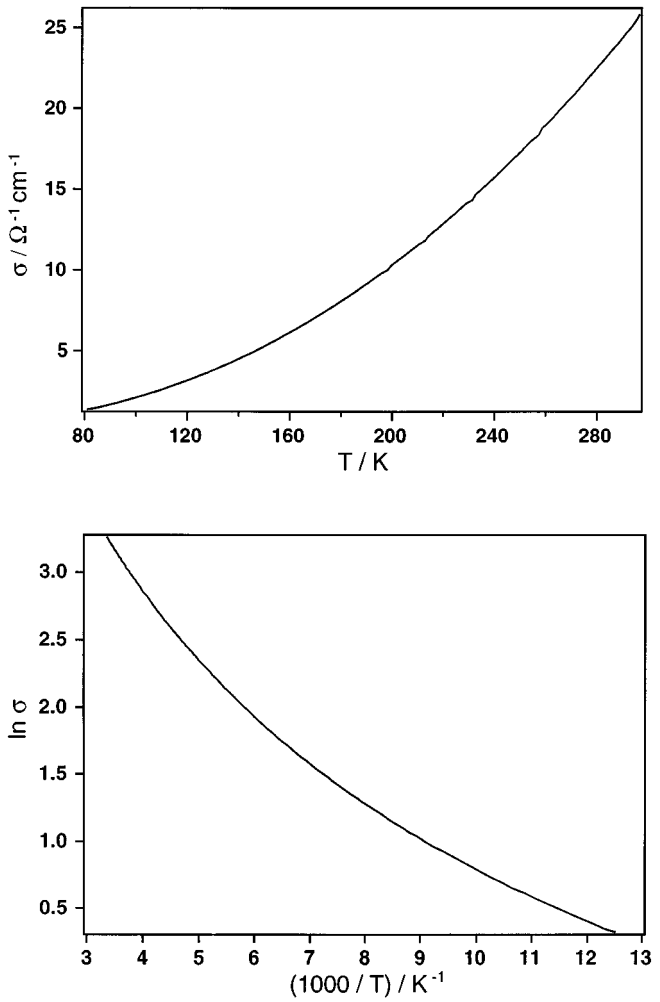

FIG. 8. Electrical conductivity of Sr_2FeIrO_6 as a function of temperature (top) and natural logarithm of conductivity versus inverse temperature (bottom).

($\sim 7\%$) of disorder present among the transition metal cations, which suggests additionally that some of the Fe cations on 2*b* sites are not fully ordered. We shall return to this point below.

When long-range antiferromagnetic ordering occurs, the dominant magnetic interaction may take place either between nearest-neighbor (NN) Fe^{3+} cations, which are ~ 5.5 Å apart, or between next-nearest-neighbor (NNN) Fe^{3+} cations ~ 7.8 Å apart. The adoption of a Type II magnetic structure indicates that the NNN antiferromagnetic interaction, along the pseudo-linear Fe–O–Ir–O–Fe superexchange pathway, is stronger than the interaction between nearest Fe neighbors along the shorter but nonlinear Fe–O–O–Fe pathway. $BaLaCoIrO_6$, in which the Co^{2+} moments align antiferromagnetically in a Type II cell, displays very similar magnetic behavior, although with a lower Néel temperature of 56 K. These two examples demonstrate that NNN magnetic interactions over long distances can sometimes be as important as or more important than nearest-neighbor interactions in determining the magnetic properties of perovskites. Therefore, descriptions of magnetic properties in perovskite structures that take into account only NN interactions should be treated with caution. It is interesting to contrast the magnetic structures of Sr_2FeIrO_6 and $BaLaCoIrO_6$ with those of the Ru(V) perovskites Sr_2MRuO_6, M = Y, Lu (17, 18), which display cation ordering and adopt Type I spin structures. In these materials, the NN Ru–O–O–Ru interactions are stronger than the NNN Ru–O–M–O–Ru interactions. The former pathway involves π-orbital overlap, whereas the latter pathway may utilize σ overlap. In the case of Sr_2MRuO_6, where the Ru^{5+} e_g orbitals are empty, overlap with the oxide p orbitals is possible only through the relatively weak π-system. The superexchange interaction along the shorter Ru–O–O–Ru pathway is therefore stronger. The NNN pathway also requires the availability of energetically accessible orbitals on the M cation. In Sr_2FeIrO_6, the requirements for σ overlap along the Fe–O–Ir-O–Fe pathway are met; the Fe^{3+} $3d$ z^2 orbital is half occupied, and the Ir^{5+} $5d$ z^2 orbital is vacant and energetically accessible. Materials in which the interactions along the two pathways are of comparable strength would be expected to adopt the Type IIIa spin structure, as is the case in Ba_2LaRuO_6 (19). However, the subtle balance between the different interactions is illustrated by the fact that Sr_2FeSbO_6 orders as a Type I magnet. It is not clear whether the differences in the magnetic behavior between this compound and Sr_2FeIrO_6 are due principally to the different degree of cation ordering (Fe:Sb = 0.795:0.205) or to the different electronic structures of the pentavalent cations.

In the above discussion we have linked the cation antisite defects to the anomalies in the magnetic data without explaining the details of the link between them. Consideration of the competing superexchange pathways allows us to offer an explanation for the spin disorder in Sr_2FeIrO_6 which relies on the presence of structural disorder. The most important superexchange interaction in the Type II spin structure is that between NNN Fe^{3+} ions, over a pseudo-linear distance of ~ 7.8 Å. A small proportion of the six-coordinate sites located halfway along this pathway will be occupied by Fe^{3+}. The magnetic moments of the Fe^{3+} cations at either end of the Fe–O–Fe–O–Fe pathway will be aligned antiparallel, as required by Type II antiferromagnetism. Ordering of the moment of an Fe^{3+} cation on the central (2*c*) site will therefore be frustrated, because it will undergo conflicting interactions with the neighboring (2*b*) Fe^{3+} cations. Even allowing for an Fe occupancy of 0.928 on the 2*b* sites and assuming a completely random distribution, some 65% of any Fe on the 2*c* sites will have configurations which are frustrated within the strict crystallographic symmetry: magnetic coupling of these sites can take place only if the

Fe–O–Fe interactions are made nonequivalent by local distortions caused by the disorder, or by interaction with more distant neighbors. Such weak couplings would only result in significant magnetic interaction with the dominant Type II lattice at temperatures far below the ordering temperature, and would also result in a marked difference in the ZFC and FC experiments at low temperatures because of a poorly defined ground state for the spin system as a whole. Furthermore, it is possible (although unproven) that the locally Fe-rich regions in $(FeO)_6Fe$ clusters could contain the Fe^{4+} cations detected by Mössbauer spectroscopy on the marginally smaller central 2*c* site and that the locally Ir-rich regions in $(IrO)_6Ir$ clusters contain paramagnetic Ir^{4+} cations on the marginally larger central 2*b* site. Alternatively, the anisotropic crystal field in $(FeO)_5(IrO)Fe$ clusters, for example, could stabilize the anisotropic Fe^{4+} d^4 species in 35% of the disordered sites. The apparent discrepancy between the site occupation from diffraction data and the oxidation states from Mössbauer spectroscopy lends some support to this suggestion. Such a deviation from the mean cation distribution would cause a local variation in the distribution of Fe/Ir–O bond lengths and would thus have a significant effect on the local superexchange interactions, possibly preventing spin ordering over a volume large enough to include local 2*b* sites. Use of these arguments allows us to relate the experimental indicators of spin frustration, that is, ZFC/FC divergence and the nonzero remnant magnetization, to B-site cation disorder, and to the complex behavior of a small fraction of the Fe spins. A more detailed study by magnetometry and Mössbauer spectroscopy will be needed before a full description of this behavior can be provided.

In conclusion, we have determined both the crystallographic and magnetic structures of the new phase Sr_2FeIrO_6. We have shown that high-resolution neutron diffraction data are sometimes required to ascertain the true crystallographic structure of perovskites when oxide ions are displaced from their ideal positions. This phase is an example of a perovskite which displays extensive but incomplete B-site cation ordering. Given the similarity of the cation sizes, as judged by the bond lengths in Table 2, and bearing in mind that the actual charges on Fe^{3+} and Ir^{5+} are likely to be very similar, it is perhaps surprising that almost complete ordering of the six-coordinate cations occurs in this material; the origin of the effect is not clear. However, the small level of imperfection in the structural cation ordering is enough to ensure that a fraction of the transition metal spins do not take part in the antiferromagnetic ordering seen below 120 K, but instead give rise to a complex hysteresis behavior. We have suggested that the cation oxidation states may change in the vicinity of the disordered sites. We have no direct evidence for this, save that Mössbauer spectroscopy shows the presence of $\sim 4\%$ Fe^{4+} somewhere in the sample.

ACKNOWLEDGMENTS

We are grateful to the EPSRC for financial support and to R. M. Ibberson for experimental assistance at the Rutherford–Appleton Laboratory.

REFERENCES

1. P.D. Battle and J. G. Gore, *J. Mater. Chem.* **6,** 1375 (1996).
2. D. Y. Jung, P. Gravereau, and G. Demazeau, *Eur. J. Solid State Chem.* **30,** 1025 (1993).
3. D. Y. Jung and G. Demazeau, *J. Solid State Chem.* **115,** 447 (1995).
4. M. Walewski, B. Buffat, G. Demazeau, F. Wagner, M. Pouchard, and P. Hagenmuller, *Mater. Res. Bull.* **18,** 881 (1983).
5. P. D. Battle, J. G. Gore, R. C. Hollyman, and A. V. Powell, *J. Alloys Comp.* **218,** 110 (1995).
6. A. V. Powell, J. G. Gore, and P. D. Battle, *J. Alloys Comp.* **201,** 73 (1993).
7. R. C. Currie, J. F. Vente, E. Frikkee, and D.J. W. Ijdo, *J. Solid State Chem.* **116,** 199 (1995).
8. P. D. Battle, T. C. Gibb, A. J. Herod, S.-H. Kim, and P. H. Munns, *J. Mater. Chem.* **5,** 865 (1995).
9. E. J. Cussen, J. F. Vente, P. D. Battle, and T. C. Gibb, *J. Mater. Chem.* **7,** 459 (1997).
10. P. D. Battle, T. C. Gibb, A. J. Herod, and J. P. Hodges, *J. Mater. Chem.* **5,** 75 (1995).
11. S. H. Byeon, T. Nakamura, M. Itoh, and M. Matsuo, *Mater. Res. Bull.* **27,** 1065 (1992).
12. P. D. Battle, T. C. Gibb, C. W. Jones, and F. Studer, *J Solid State Chem.* **78,** 281 (1989).
13. A. C. Larson and R. B. von-Dreele, "General Structure Analysis System (GSAS)," Los Alamos National Laboratories, Report LAUR 86-748, 1990.
14. P. J. Brown, Magnetic scattering of neutrons, *in* "International Tables for Crystallography" (A. J. C. Wilson, Ed.), Vol. C, Kluwer, Dordrecht, 1995.
15. R. A. Tahir-Kheli, H. B. Callen, and H. Jarret, *J. Phys. Chem. Solids* **27,** 23 (1960).
16. B. C. Tofield and B. E. F. Fender, *J. Phys. Chem. Solids* **31,** 2741 (1970).
17. P. D. Battle and C. W. Jones, *J. Solid State Chem.* **78,** 108 (1989).
18. P. D. Battle and W. J. Macklin, *J. Solid State Chem.* **52,** 138 (1984).
19. P. D. Battle, J. B. Goodenough, and R. Price, *J. Solid State Chem.* **46,** 234 (1983).